Acetone PLIF visualization of the fuel distribution at plasma-enhanced supersonic combustion

Skye Elliott [a],[*], Philip Lax [a], Sergey B Leonov [a], Campbell Carter [b], Timothy Ombrello [b]

[a] *University of Notre Dame, Notre Dame, IN, 46556, USA*
[b] *Wright-Patterson Air Force Base, OH 45433, USA*

ARTICLE INFO

ABSTRACT

This study examines the mixing and flameholding characteristics of a plasma stabilized planewall supersonic combustor. Fuel injection, ignition, and flameholding are provided by Plasma Injection Modules (PIMs) installed in a $M = 2$, 76.2×76.2 mm duct. Two configurations were explored: the first involves a plasma filament collocated within a single transverse fuel jet, while the second involves combustion stabilization using a series of three PIMs. Unburned fuel distributions were assessed with acetone planar laser induced fluorescence (PLIF), where acetone vapor was seeded into the gaseous fuel. PLIF measurements were performed for both streamwise and spanwise laser sheet orientations. Supporting datasets were collected including schlieren imaging, chemiluminescent imaging, and pressure distributions. PIM actuation is found to increase jet penetration, crossflow expansion, and initiate fuel jet breakup. The average jet cross sectional area is shown to increase by >20% with the addition of plasma. PLIF imaging at PIM stabilized combustion revealed a significant unburned fuel concentration in a local separation region near the PIMs, and identified the minimum plasma pulse duration for flowfield transition from initial conditions to the combustion pattern.

1. Introduction

Demand for high-speed airbreathing propulsion systems has led to intense study of the mixing and ignition dynamics of directly injected fuel in supersonic flows [1,2]. The short residence time in a practical-length combustor makes sustained combustion challenging as fuel–air mixing must occur on a molecular level before ignition, and flame propagation speed is orders of magnitude below the freestream gas velocity. This is especially true at engine startup or after a loss of thrust event (unstart, blowoff, etc.) where the conditions for autoignition may not be met. Mechanical devices, such as pylons [3,4] and cavities [5,6], blockage and shock-wave-based approaches such as transverse jets [7], and electric discharges [9,10,11], are employed to create subsonic recirculation zones where increased residence times allow for mixing and initiation of local combustion zones. The heat release and radical production in these regions may then initiate bulk combustion in the core flow.

There are several challenges associated with the design of fuel injector systems for rapid fuel–air mixing in supersonic flows. Gas compressibility suppresses turbulence, mixing layer growth rate, eddy formation, and eddy breakup. This has been shown through reduction of the shear layer growth rate with increasing convective Mach number in several experimental and numerical studies [12,13]. Exothermic reactions have been shown to further affect mixing in compressible flows [14], although to less effect than in subsonic flows. Mixing enhancement is typically achieved through the introduction of vorticity to interact with the fuel–air layer, or active excitation of large-scale structures [15]. This includes intrusive changes to combustor geometries [8] (swept ramps, injector orifice shapes, injection angles etc.), and active methods such as pulsed jets [16] or acoustic excitation [17] among others.

The flameholding approach of interest for this work includes use of the plasma injection module (PIM) [11]. This approach combines the generation of a quasi-DC (Q-DC) plasma with fuel injection to allow for targeted energy deposition in fuel–air mixing regions [18]. Previous studies in a plane wall geometry [11,19] showed PIM operation can provide stable flameholding across a wide range of stagnation pressures and temperatures, while minimizing total pressure losses once conditions for autoignition are met and the electrical discharge may be turned off. It is not clear, however, what the specific mechanisms are (mixing intensification, fuel preconditioning, thermal addition, etc.) that combine to yield the extension of flameholding limits seen in previous tests [20]. This study focuses on two key aspects of the PIM system: (1)

---

* Corresponding author.
E-mail address: selliot4@nd.edu (S. Elliott).

mixing characteristics of the PIM compared to conventional transverse fuel injection and (2) the fuel pattern at combustion initiation at three-PIM operation.

Planar laser-induced fluorescence (PLIF) is a commonly used technique for the study of supersonic reacting and non-reacting flows. While hydrocarbon combustion contains chemical species that may be probed for mapping of reaction zones, heat release areas and scalar quantities, such as gas temperature and number densities, [21,22,23,24], non-reacting flows typically require the addition of a tracer molecule for measurements and visualization. Though many tracer candidates have been explored [25,26], acetone is frequently selected in fuel–air mixing studies. It may be used both before chemical reactions, to identify fuel-rich regions, and during combustion to identify unburned fuel areas where acetone photophysics has not been affected by chemical reactions. The popularity of acetone as a tracer is due to its favorable characteristics: acetone has a broad absorption band for excitation from the ground state to the first excited singlet state centered around 275 nm, which is accessible by the 4th harmonic of Nd:YAG lasers. It is characterized by negligible collisional quenching due to a short fluorescence lifetime (for excitation between 260 and 280 nm, $t < 2$ ns [27]), and by a reasonable fluorescence yield of around 0.2% [28]. Additionally, it has a high vapor pressure ($\sim$0.3 bar at 298 K) for simple seeding into gas flows. Because of this, acetone has been widely used in subsonic and supersonic combustion studies [29,30,31]. However, there is also a factor preventing the use of acetone as a tracer in a cold supersonic flow: condensation at low static temperature.

The current study applies acetone PLIF to directly visualize the pattern of gaseous fuel injection into a model scramjet combustor before, at, and after the application of an electric discharge. This allows for direct characterization of the plasma impact on fuel–air mixing and indicates under what conditions the plasma localizes in favorable regions of the injected jet. Data were collected in a plane wall combustor geometry under varying fuel mass flowrate, plasma power, and flow parameters. Section 2 describes the experimental facility, acetone PLIF apparatus and acetone condensation control methods, Section 3 describes single PIM operation, Section 4 describes the fuel pattern of a three-PIM system at strong combustion and Sections 5-6 present discussion and key conclusions of the work.

2. Experimental approach

2.1. Facility and instrumentation

The supersonic, M = 2, blowdown wind tunnel SBR-50 at the University of Notre Dame was used in this study. In this work the origin for all indicated distances is at the PIM exit as indicated in Fig. 1. In the current configuration, the facility simulates a high-speed combustor with an initial cross section of $\Delta z \times \Delta y = 76.2 \times 76.2$ mm, a total length from the nozzle exit to the diffuser of $\Delta x = 610$ mm, and a 1° expansion of the top and bottom walls to account for boundary layer growth and mitigate thermal choking during combustion. In the plenum, electrical preheating was used to vary stagnation temperature from $T_0 = 297–550$ K, and stagnation pressure from $P_0 = 1–2$ bar, providing a steady-state runtime of $t > 0.5$ s. The sidewalls of the test section are equipped with quartz windows for optical observations and a bottom insert with optical access was used for select runs to obtain top-wall normal images of plasma/flame structure. Forty-eight pressure ports are distributed along the top and bottom walls, and a 16-probe stagnation Pitot rake is located at the end of the test section.

Standard instrumentation includes a 64-channel pressure scanner (Scanivalve MPS4264, $\pm$0.06% Full Scale Output) with an 800 Hz scanning rate, and a high speed schlieren system, backlit with a high intensity pulsed diode (Luminus CFT-90-W) with a pulse duration of $t = 200$ ns. Schlieren images were collected using a Phantom V2512 high speed camera with a fixed exposure time of 260 ns and framerate of 50 kHz. Spectral filtering was applied using a 450 nm long-pass filter to prevent plasma-related overexposure of the camera sensor. Fast imaging of the plasma filament structure was performed using a Photron Fast-Cam Nova S9 at framerates between 25 and 100 kHz with exposure times of 4 μs. A schematic of the upper wall of the test section is shown in Fig. 1a, with conditions and instrument ports labeled. A schematic of fuel injection in relation to laser sheet forming is shown in Fig. 1b.

The ignition system applied in this work consisted of three PIMs installed in a planewall configuration with transverse gas injection. A simplified cross-section drawing of a PIM is shown in Fig. 2 along with a schematic of PIMs installed into the test section wall. PIM construction consists of a metal tubular electrode with internal diameter $d_{inj} = 3.2$ mm fixed in a ceramic insulator. A high voltage is applied to the
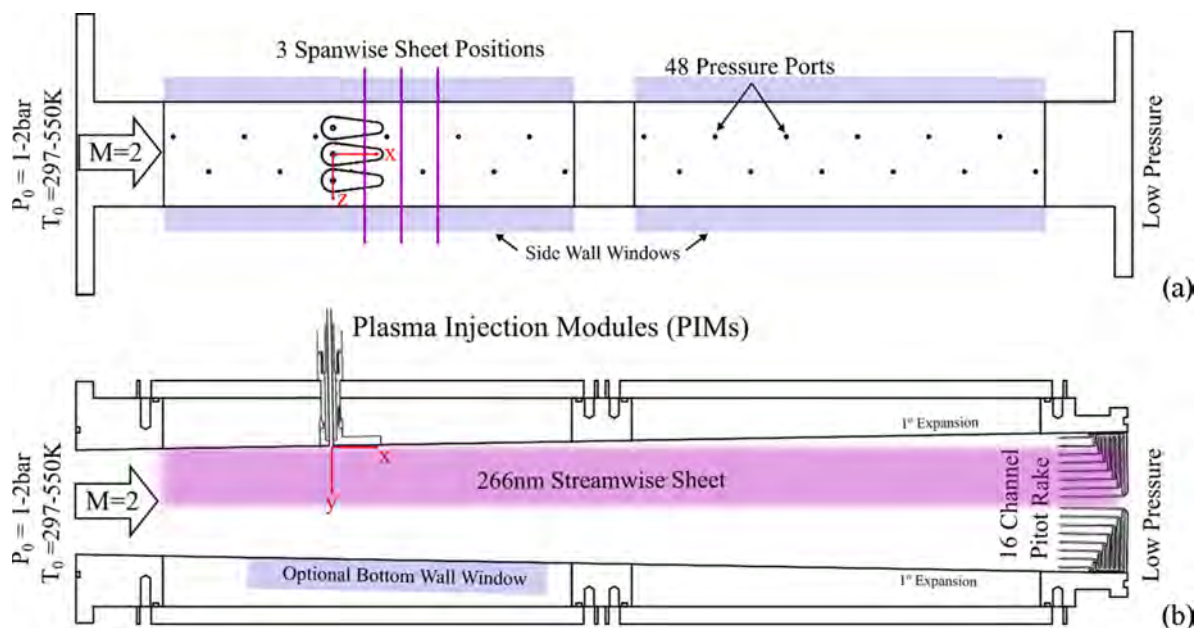

Fig. 1. Schematic of the test section where (a) shows a wall normal view of the upper wall with pressure ports and spanwise laser sheet positions and (b) shows the location of the PIMs and the streamwise laser sheet.
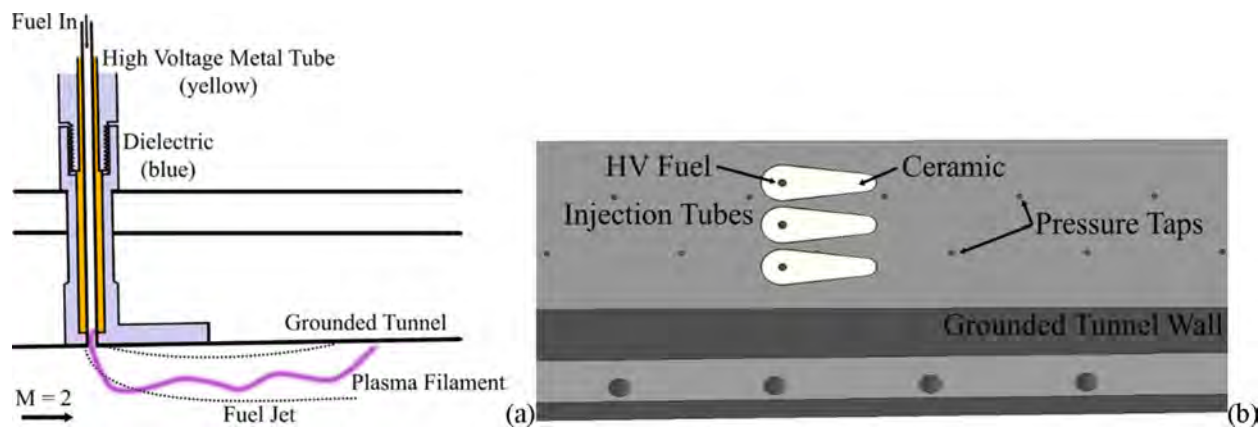
Fig. 2. (a) Plasma Injection Module (PIM) schematic; (b) 3D schematic of plane wall test section with PIMs.

electrode, which also serves as the fuel injection port, the fuel being ethylene in the case of three PIMs fueled or an ethylene + methane blend (64% C2H4, 36% CH4) used in this work for a single PIM fueled. The wall facing shape of the ceramic is designed to assist in elongating the filament with the flow and the PIMs are evenly distributed $\Delta z_{PIMS} = 25.4$ mm from each other and 12.7 mm from the side walls.

The electrical discharge nature is "arc-in-the-flow," which is significantly different than a conventional arc discharge due to strong coupling of the constricted plasma to the high-speed flowfield [20]. This discharge is powered by a Direct-Current (DC) power supply and is characterized by an essential unsteadiness from regular displacement of the plasma filament in the external flow direction. This leads to the terminology "Quasi-DC" (Q-DC) discharge. Power supply design allows for current-stabilized operation with a fixed ballast resistor connected in series with the PIMs. Probes at the output of the power supply and across voltage gaps allow for calculation of Q-DC discharge parameters including plasma power. Average plasma power for this work was in the range of W = 3–5.4 kW per PIM with typical voltages of U = 500–700 V and currents of I = 6–8.6A. Plasma filaments display unsteady behavior due to downstream filament convection leading to a critical length of the filament being reached, wherein a new filament forms upstream of the previous one. Gas temperature in the plasma filaments has been measured by optical emission spectroscopy in the range of 4-6kK [32].

2.2. Acetone PLIF setup

When using acetone as a tracer in reacting flows, three main features should be taken into account:

1. Pyrolysis: acetone starts pyrolyzing at temperatures >1000 K: the rate of the pyrolysis reaction increases with increasing temperature and pressure [33]. The pyrolysis time constant at 1 bar and 1250 K is about 50 ms [29], which is much longer than residence times in the combustor for this work.
2. Preferential diffusion: acetone $(CH_3)_2CO$ has a molecular weight $M_{ace} = 58.08$ g/mol while for nitrogen $M_{N2} = 28.01$ g/mol and for ethylene $M_{C2H4} = 28.05$ g/mol. As the diffusivity coefficient varies as $D \propto 1/\sqrt{M}$, acetone will diffuse slower than the seeded gas. The magnitude of this effect can be considered through the Damköhler number, where at small values the chemical reaction occurs after molecular mixing of the reactants. It was found to be negligible in the current configuration. Same conclusion is valid for the ethylene-methane fuel blend (64% C2H4, 36% CH4) used for a single PIM testing.
3. Heat release: for acetone the enthalpy of combustion is $\Delta_c H_{ace}^\circ = -1.82$ M J/mol while for ethylene $\Delta_c H^\circ_{C2H4} = -1.40$ MJ/mol. The maximum molar concentration of acetone used in this work is 12%

which would yield up to about a 3.5% difference in $\Delta_c H^\circ$. This difference is acceptable for qualitative imaging.

These factors indicate that in small Damköhler number flows where the residence time and temperature are not high, the effects of pyrolysis and preferential diffusion will be minimized. Pressure and temperature dependence of the acetone fluorescence yield must also be considered. Minimal change in acetone fluorescence is seen across the pressure differences present in this work, but the change with temperature is approximately an 8% decrease in the acetone PLIF signal per hundred Kelvins [34]. Practically, this limits acetone PLIF measurements in a reacting flowfield to qualitative assessments, as areas of high heat release correspond to both acetone destruction by combustion, and signal decrease due to temperature effects and volumetric expansion. As unburned fuel areas remain at low temperature near fuel injection (before significant mixing), they are still readily identified. A final consideration for both reacting and non-reacting acetone PLIF studies is acetone nucleation due to low static flow temperatures. This is addressed in Section 2.3. The experimental conditions for this work are favorable for qualitative acetone PLIF imaging.

There are two key components of the acetone PLIF system: the seeding system, and the laser sheet arrangement. Liquid acetone kept at T = 297 K and monitored using a type-C thermocouple was premixed with gaseous fuel using a long tubular bubbler to achieve a saturated concentration of vapor in the carrying gas. The mixture was then routed to a fuel canister where injection pressure was set. This allowed for variation of the acetone concentration based on seeder pressure, and variation of the fuel mass flow rate based on fuel canister pressure. The mixture was then injected at mass flowrates in the range of $\dot{m} = 0$–4 g/s through the PIMs with a typical acetone concentration of 5–12%.

Acetone excitation was provided by the 4th harmonic of a Quanta-Ray DCR-4 pulsed Nd:YAG laser ($\lambda = 266$ nm) with a pulse repetition frequency of 10 Hz and pulse energy at 266 nm of up to 70 mJ. The optical arrangement resulting in 4th harmonic generation and sample sheet forming is shown in Fig. 3. The distance between the laser output and point of observation varied from approximately 0.5 m to 3 m depending on the sheet orientation (streamwise vs spanwise).

Two laser sheet orientations were explored, a streamwise sheet entering through a fused silica window in the vacuum tank and bisecting the test section along with the central PIM, and a spanwise sheet at three different downstream locations from the PIMs. In the streamwise scheme, the long focusing distance (>2.5 m) made traditional two lens sheet forming arrangements impractical, and the laser sheet was formed using a plano-convex spherical lens (f = 3 m) with two cylindrical lens (f = 500 mm, f = -100 mm) to create a diverging laser sheet with a height of approximately h = 40 mm and a thickness of approximately $\Delta w = 2$ mm at the PIMs location.

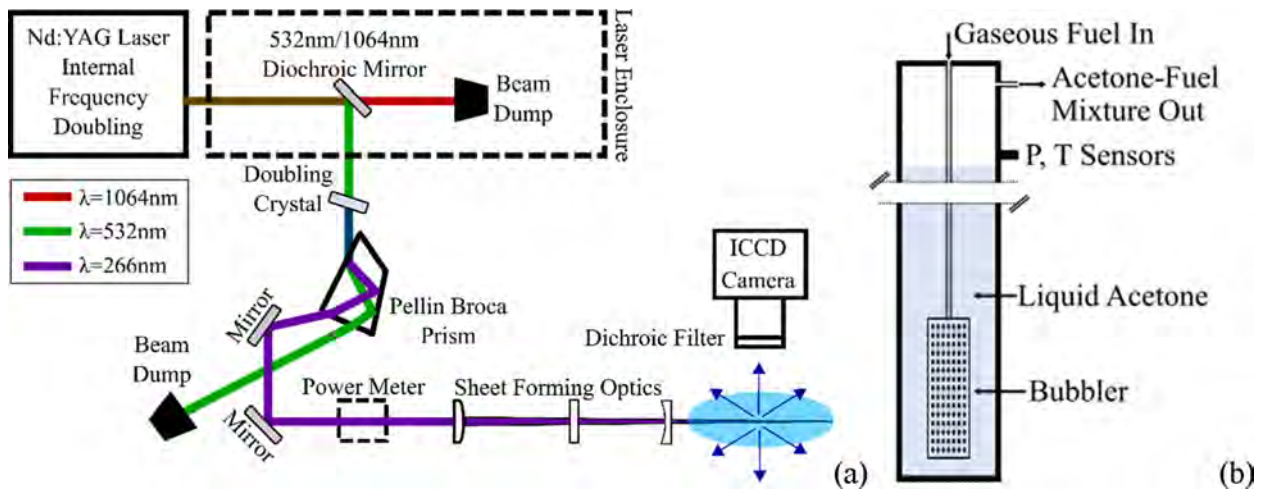In the spanwise scheme, the laser sheet entered the test section

Fig. 3. Acetone PLIF system components where (a) shows Nd:YAG laser frequency conversion and laser sheet forming and (b) shows the acetone seeding system.

through the side windows and three downstream locations were explored, x = 25, 50 and 75 mm downstream of the PIMs, which correspond to x/d_{inj} = 7.8, 15.6 and 23.4. Short focusing distances in this arrangement allowed for simple sheet forming using a spherical plano-convex (f = 500 mm) and cylindrical plano-concave (f = -100 mm) lens arrangement providing a collimated laser sheet with a height of h = 40 mm and thickness Δw = 600 µm at the centerline of the test section. Imaging of the laser sheet was performed through the vacuum port window, leading to decreased spatial resolution and signal in the spanwise images. Non-uniformities of the laser sheet were accounted for in both schemes by collecting in situ images with a uniform seeding of acetone in the test section to use for image processing and to assess sheet characteristics.

Imaging of acetone fluorescence was performed with two different camera arrangements: (1) a PCO DiCam C1 was applied with an exposure time of 200 ns for the single PIM mixing study, and (2) a Lambert HiCATT optical relay intensifier with an exposure time of 20 ns was coupled to a Phantom V2512 high speed camera with an exposure time of 260 ns for three PIM fuel–air mapping during combustion. The image acquisition frequency in both arrangements was fixed by the laser system at 10 Hz. Timing for the facility was set by two Berkeley Nucleonics pulse delay generators (Model 577) which coordinated all diagnostics and tunnel operations. Laser pulse timing was controlled with a photosensor.

2.3. Acetone condensation control

Acetone condensation at low gas temperatures is a common issue that can prevent deployment of acetone PLIF for supersonic flow diagnostics. The SBR-50 facility provides unique capabilities to apply this diagnostic technique due to a precise control of stagnation temperature. A plot of the saturation ratio (S) of acetone with variation of the facility stagnation temperature is shown in Fig. 4a, where S = 1 dividing unsaturated and supersaturated acetone is highlighted red. The saturation ratio is shown for two cases: (1) in front of the bow shock and (2) across a 20° oblique shock wave: two cases that bound the conditions at jet injection. Note, the normal shock portion of the bow shock would result in a more conservative "bounding" of conditions, that the majority of the flowfield behind the bow shock does not experience. Conditions for these cases were calculated using isentropic flow relations. Where S≫1 homogeneous condensation appears, and where S < 1, homogeneous condensation cannot occur. This predicted onset region was then validated using PLIF signal data.

A complementary experimental dataset was collected by varying the main airflow stagnation temperature in the range of T_0 = 297–550 K. At each condition, four PLIF images were collected with subsequent background subtraction and image normalization to account for the laser distribution. An average image was then assembled at each T_0. Mean pixel values at the jet exit in a $\Delta x \times \Delta y = 6.4 \times 4.4$ mm region comprised of 1750 pixels were then taken for each case to minimize flowfield effects when comparing across values. All data were then
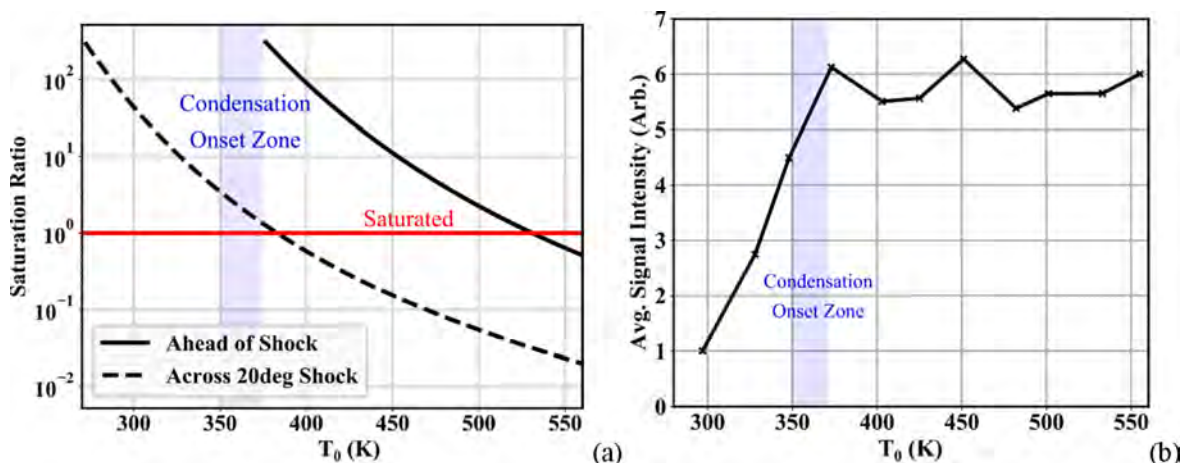

Fig. 4. Comparison of (a) the saturation ratio of acetone with variation of T_0 and (b) the PLIF signal intensity at the jet exit with variation of T_0.

normalized to the value at 297 K. Error is estimated to be ±10% of the calculated mean values based on the small image sample size and sensitivity of the mean value to the jet exit region. Fig. 4b shows the resulting variation of signal as temperature changes, where the signal stays constant within the error until at $T_0 < 375$ K the value drops suddenly in the corresponding region to predicted condensation onset. This indicates the effect is due to condensation of acetone in the flow, where any resulting Mie/Rayleigh scattering signal is minimized by spectral filtering of the glass camera lenses. For the single PIM mixing study, a stagnation temperature $T_0 = 450$ K was selected to prevent homogenous condensation and maximize the PLIF signal. For the three-PIM combustion study, a stagnation temperature of 297 K was used to produce stable flameholding with the highest combustion intensity [11]. At intensive combustion significant flow separation produces conditions that mitigate acetone condensation. At baseline flow cases the signal remained sufficient to establish the fuel-jet pattern.

3. Single-PIM mixing results

A dataset was first collected to characterize the effect of plasma impact on the penetration and expansion of a transverse fuel jet. Fuel injection was only provided through the central PIM, and an ethylene-methane fuel blend (64% C_2H_4, 36% CH_4, used to simulate the reactivity of cracked JP-7 [35]) was applied. Lower reactivity of the fuel and single PIM actuation prevented strong combustion modes from developing in the test section and producing significant flowfield changes. By limiting the effects of heat release due to combustion, the effect of plasma impact on the fuel jet was explored.

Transverse gas penetration depth into a supersonic flow is primarily dependent on the momentum flux ratio (J).

$$J \equiv \frac{\rho_j U_j^2}{\rho_\infty U_\infty^2} = \frac{\gamma_j p_j M_j^2}{\gamma_\infty p_\infty M_\infty^2} \quad (1)$$

where the subscripts ∞, j represent freestream and injected jet quantities respectively [7,36,37]. Three different momentum ratios were selected, J = 0.75, 1.2 and 2.1, through variation of the facility stagnation pressure and fuel injection pressure. Acetone concentration was fixed at 5% across this series. Distances in presented figures are non-dimensionalized by the PIM injector diameter, d_{inj}, to allow comparison with prior works.

3.1. Single PIM baseline and plasma modified flowfield characterization

Measurement of the pressure distribution and schlieren imaging were performed at test conditions with baseline flow, fuel injection, and fueling with plasma actuation. Fig. 5 shows schlieren images collected at fuel injection cases with and without plasma actuation. Without plasma

actuation the shock wave related to fuel injection and the shear layer resulting from the transverse injection into supersonic flow are seen. The strong bow shock originates at the injection point, inducing the flow separation zone just upstream of the PIM location. The large density gradient at the jet exit produces the visible dark region. A barrel shock structure at injection is visible and a significant amount of fluid penetrates between the upstream edge of the barrel shock and the bow shock, as observed in previous studies [31]. When the electric discharge is actuated on, the plasma filament is seen to locate in the injected jet, intensifying density gradients near the jet boundary and increasing jet penetration depth, see Section 3.2. Breakdown occurs at the downstream edge of the PIM port, causing the plasma filament to locate downstream of the barrel shock and interact with the counter-rotating vortex pair generated in the jet [18]. This behavior generates the helical shape of the plasma filament.

Static pressure distributions along the top wall and stagnation pressure distributions at the end of the test section are presented in Fig. 6 at baseline flow, fueling and fueling with plasma. The largest pressure increase is seen in the case of fueling with plasma, where plasma generation leads to electrical heat release in the jet. This heating causes the formation of a subsonic zone which acts as a virtual obstacle that increases oblique shock strength and causes the downstream reflection seen at $x/d_{inj} \approx 78$. This effect is similarly seen in stagnation pressure rake data in Fig. 6b, with the result that the boundary layer on the top wall is more developed, as indicated by the stagnation pressure decrease near the top wall.

3.2. Streamwise single PIM fuel pattern

Acetone PLIF imaging was performed with the streamwise laser sheet arranged along the centerline of the test section ($z/d_{inj} = 0$) to visualize differences in the fuel distribution with and without plasma actuation. The outer boundary of the jet was identified by scanning images starting in the core flow at $y/d_{inj} = 9$ and progressing in the negative y-direction until 5 times the average background value was reached. Radiative lifetimes for the main transitions responsible for optical emission from the plasma are on the order $\tau_{rad} = 10^{-6}$-10^{-8}s, while some decay in current at plasma off slightly extends this time. To prevent plasma related saturation of PLIF images due to the disparate intensity scales, yet still capture plasma's impact on the flowfield, images at plasma cases were collected at $t_{delay} = 10$–30 μs after a 10 ms duration plasma pulse was actuated off. Some variation in this timing was due to the laser-timing jitter. A non-transparent mask was placed parallel to the top wall to crop fluorescence from ceramic PIM components.

Fig. 7 shows a false color image comparison of processed PLIF images for cases of jet injection with and without plasma actuation. In Fig. 7a and b, single-shot images are shown, and in Fig. 7c,d average images are shown composed of 6 single-shot images. In the images, the intensity
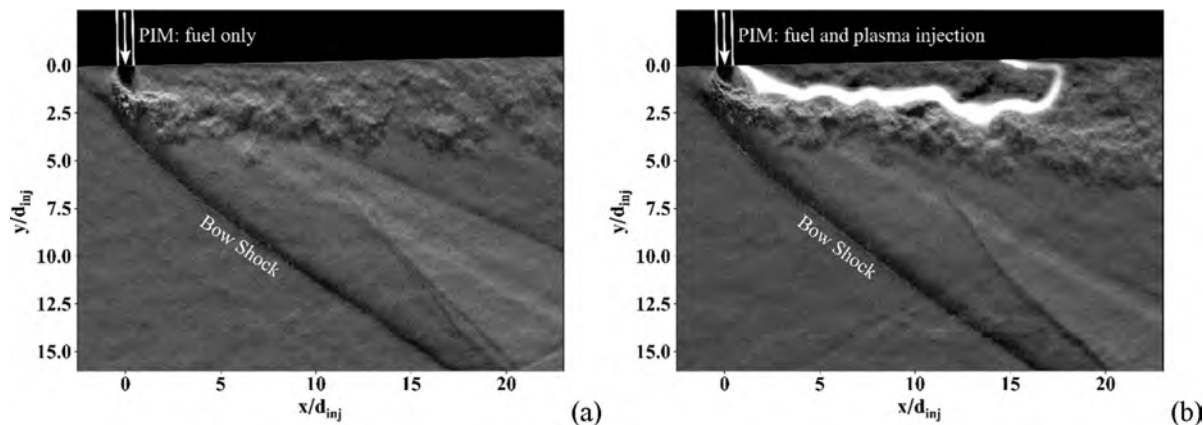

Fig. 5. Single schlieren images where (a) shows a single PIM fueling case before plasma and (b) shows a single PIM operating in fuel.
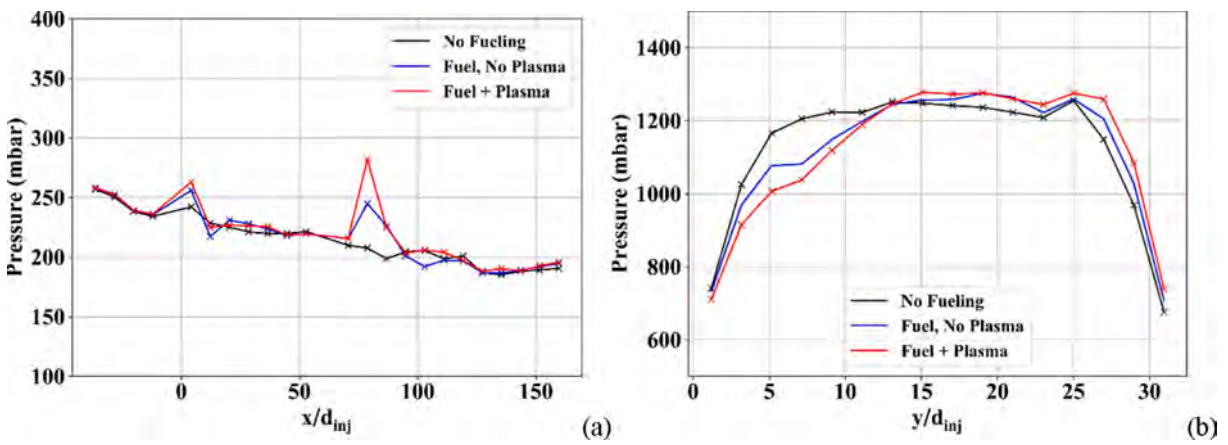
Fig. 6. Single PIM operation pressure distributions (a) shows the static pressure distribution on the top wall at three cases and (b) shows the total pressure distribution at the end of the test section at three cases.
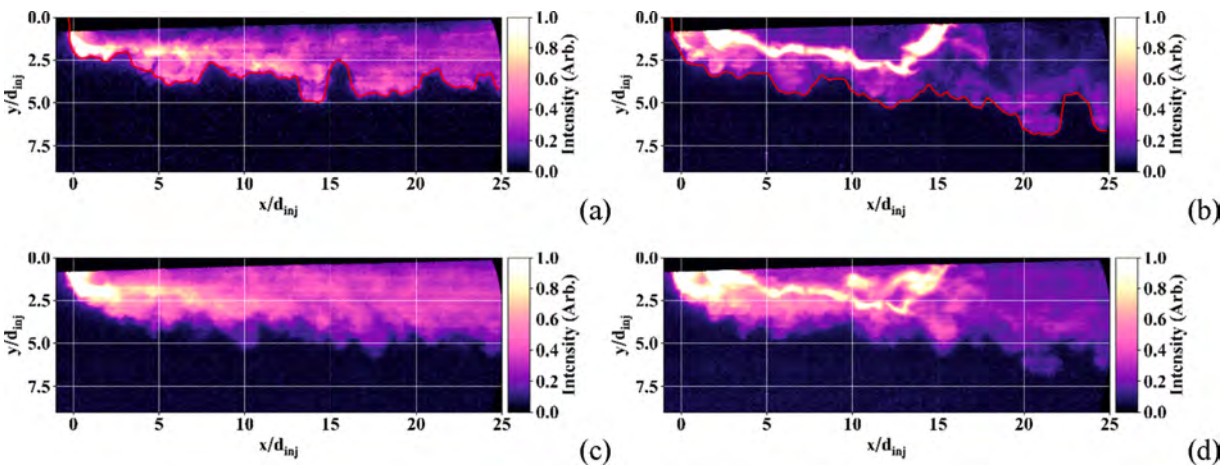

Fig. 7. False color streamwise images of an acetone seeded ethylene-methane fuel jet at a momentum flux ratio of $J = 1.1$ where (a) and (b) show single shot images of the jet before plasma and 10 μs after extended plasma impact respectively with edge finding processing and (c) and (d) show averaged images of the jet before and 10–30 μs after plasma impact respectively.

scale is adjusted as $I_{adj} = C*I_{orig}^{\gamma}$, where I_{orig} is the original signal acquired by the camera, $C = 2$ and $\gamma = 2/3$. In Fig. 7a, the jet structure is seen before plasma impact, where high shear in the fuel–air mixing layer causes rollup and the downstream development of large-scale coherent structures. A significant portion of fluid bypassing upstream of the barrel

shock, as observed in schlieren imaging, is also seen in PLIF images before plasma actuation. In Fig. 7b, acquired 10 μs after termination of plasma actuation, some significant structural differences are visible. Post-luminescence from the plasma filament informs its position without image saturation. A dark region downstream of the plasma filament
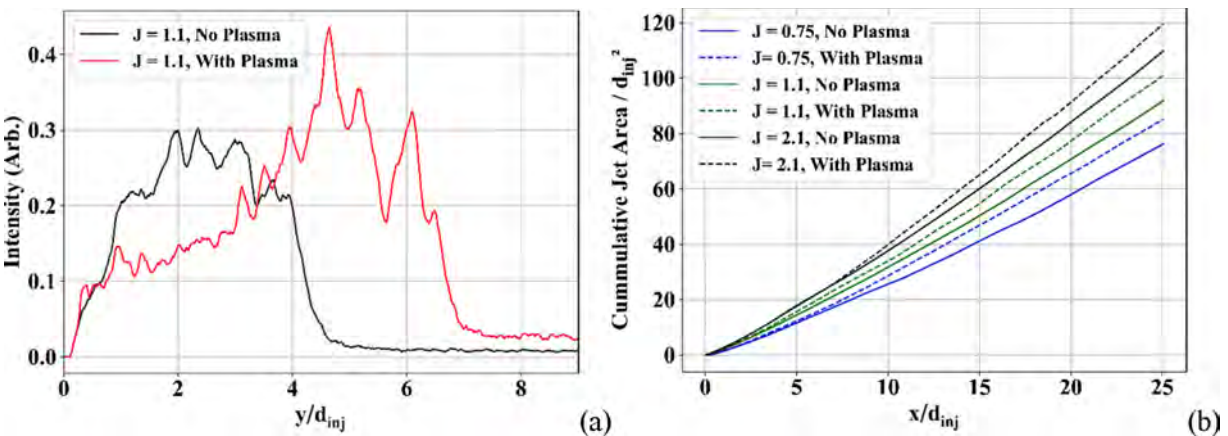

Fig. 8. Plasma effect on injected jet where (a) is the PLIF signal intensity distribution averaged over the region downstream of plasma, $x/ d_{inj} = 10–15$ mm and (b) shows a comparison of cumulative jet area in plasma vs. no plasma cases at each momentum flux ratio.

location indicates a lower concentration of acetone, this is due primarily to dissociation of acetone from plasma impact in the region and a volumetric expansion of the jet at plasma heating. The amount of fuel bypassing the barrel shock and passing upstream between the bow shock and barrel shock has decreased due to modification of the barrel shock structure, see Section 5 for details. Finally, greater jet penetration at the outer boundary is seen, especially as the jet develops further downstream. This difference in downstream jet penetration and structure was assessed for the images shown in Fig. 7 by averaging the intensity of each image at $x/d_{inj} = 19–25$. The result is shown in Fig. 8a, where both the increase in downstream jet penetration and the decrease in near-wall signal due to plasma impact are highlighted. In Fig. 7c, an average image is shown in the no plasma case, composed of 6 single-shot images. This image shows uniform downstream development of the jet and highlights the significant portion of fluid passing between the upstream portion of the barrel shock and the bow shock. In Fig. 7d an average image is shown composed of images collected between $t_{delay} = 10–30$ μs after extended plasma impact. Similar features are generally observed as described from the single-shot image in Fig. 7b. However, there is now a more significant portion of fuel passing between the upstream portion of the barrel shock and bow shock. This is due to the fact that in images collected at longer delays some portion of the plasma effect has convected downstream.

To better assess PIM behavior on mixing enhancement, outer profiles were assembled and averaged for cases with and without plasma impact at each momentum flux ratio. The cumulative jet area was then calculated by numerically integrating under each average profile. Fig. 8b shows the cumulative jet area at each J with and without the plasma effect. In the immediate area of the PIM injectors, $x/d_{inj} < 5$, a

significant difference is not apparent between the two cases; however, at $x/d_{inj} > 10$ when the jet is more developed, separation between the cases starts to occur. At $x/d_{inj} = 25$, a jet area increase due to improved penetration of $\sim 10\%$ is seen across all momentum flux ratios.

3.3. Spanwise single PIM fuel pattern

Streamwise acetone PLIF imaging of the jet allows for determination of the penetration characteristics at plasma impact, but it does not provide a complete view of the mixing characteristics as the overall fuel–air interaction surface may also be affected by spanwise expansion of the jet. To capture this effect, spanwise acetone PLIF imaging was performed at matching momentum flux ratios and stagnation conditions to the streamwise data presented in Section 3.2. Fig. 9 shows averaged false-color processed PLIF images collected at two momentum flux ratios, each with and without plasma actuation. Images shown represent the average of 28 images at each condition and are located at $x/d_{inj} = 23.4$ downstream of the PIMs. In Fig. 9a and c showing the baseline case, a circular structure with a uniform intensity is seen, indicating a uniform expansion of the jet. In Fig. 9b and d, post luminescence from the plasma obscures the PLIF signal in the center of the jet, but a more expanded less consistent outer structure is seen at both momentum flux ratios. This larger cross-sectional area includes both the deeper cross flow penetration seen in streamwise imaging, but also spanwise expansion of the jet. A comparison between average areas calculated at low and high momentum flux ratio and two spanwise positions is shown in Table 1. Jet cross-sectional areas were calculated from averaged PLIF images by counting pixels with 5 times the background intensity. In all cases plasma impact is considered to significantly increase the cross-sectional
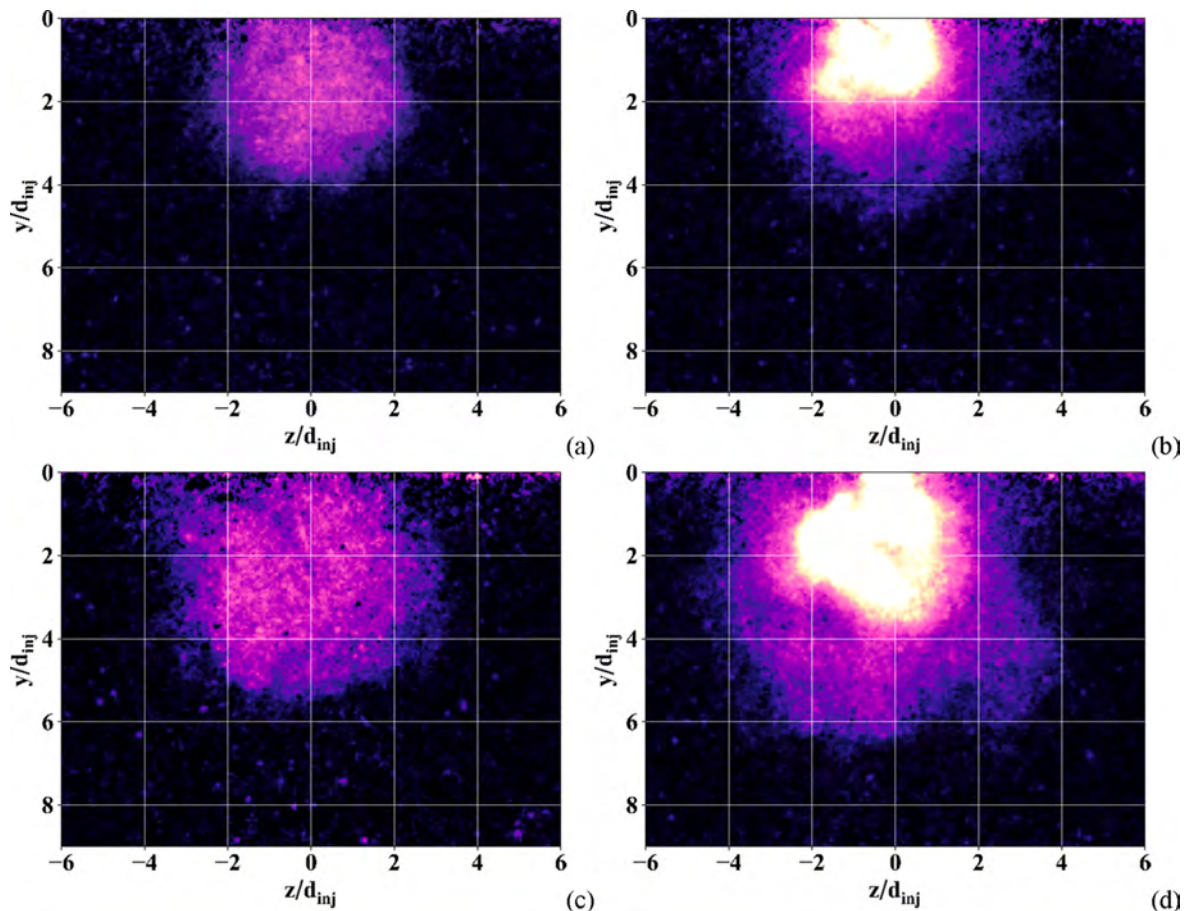

Fig. 9. Comparison of averaged PLIF images collected $x/d_{inj} = 23.4$ downstream of PIMs where (a) J = 0.75 no plasma, (b) J = 0.75 with plasma, (c) J = 2.1 no plasma, and (d) J = 2.1 with plasma.

Table 1

Averaged jet cross sectional areas for J = 0.75 and 2.1 at x/d_{inj} = 7.8 and 23.4, with and without plasma.

| Cross Sectional Area Comparison	x/d_{inj} = 7.8 Baseline	x/d_{inj} = 7.8 With Plasma	Percent Difference	x/d_{inj} = 23.4 Baseline	x/d_{inj} = 23.4 With Plasma	Percent Difference
J = 0.75	94 mm^2	124 mm^2	27%	186 mm^2	230 mm^2	21%
J = 2.1	279 mm^2	346 mm^2	21%	324 mm^2	413 mm^2	24%

area of the jet.

While average spanwise PLIF images show an enhancement of fuel–air mixing due to improved expansion and penetration of the jet, they miss an important effect visible in single-shot spanwise images, jet breakup. Fig. 10 shows representative single-shot PLIF images collected with and without plasma impact. Note that bright dots in the image are resulted from an electronic noise at high intensifier gain. While the jet structure retains a nearly circular shape in single-shot images without plasma impact, Fig. 10a, with plasma impact highly unstable behavior is observed along with a pocketed PLIF signal, Fig. 10b and c. As signal decrease due to dissociation and expansion from plasma is contained closer to the wall (see Fig. 7b), and this signal decrease is observed out to the jet boundary in Fig. 10b, this indicates jet breakup is occurring. This behavior is beneficial for mixing as it increases fuel–air interaction surfaces and entrains oxidizer into rich regions at the jet core. This behavior also indicates that the averaged cross-sectional area comparisons in Table 1 may underestimate the influence and potential benefit of plasma on mixing enhancement. This will be further discussed in Section 5.

4. Three PIM fuel pattern at combustion

For this dataset all three PIMs were activated and ethylene fuel was seeded with acetone vapors. All runs were performed at a single set of stagnation conditions, T_0 = 297 K, P_0 = 1.7 bar, and the fueling rate was fixed at $\dot{m}$ = 3.75 g/s with a cumulative momentum flux ratio of 0.6. The establishment and extinction of the strong combustion pattern was investigated by varying the plasma duration and image delay after plasma. Complementary pressure, schlieren, chemiluminescent imaging and electrical datasets were acquired in addition to acetone PLIF imaging.

4.1. Baseline and combustion mode characterization

Fig. 11 shows single-shot schlieren images collected at two different delay times after plasma actuation. In Fig. 11a, a partial oxidation mode is shown where three PIMs are actuated but flowfield transition to the combustion pattern has not yet occurred. Intense density gradients due to hot plasma filament interaction with the jet produces a shallow combustion wedge with a corresponding strong oblique shock. In Fig. 11b, transition to strong combustion has now taken place. The
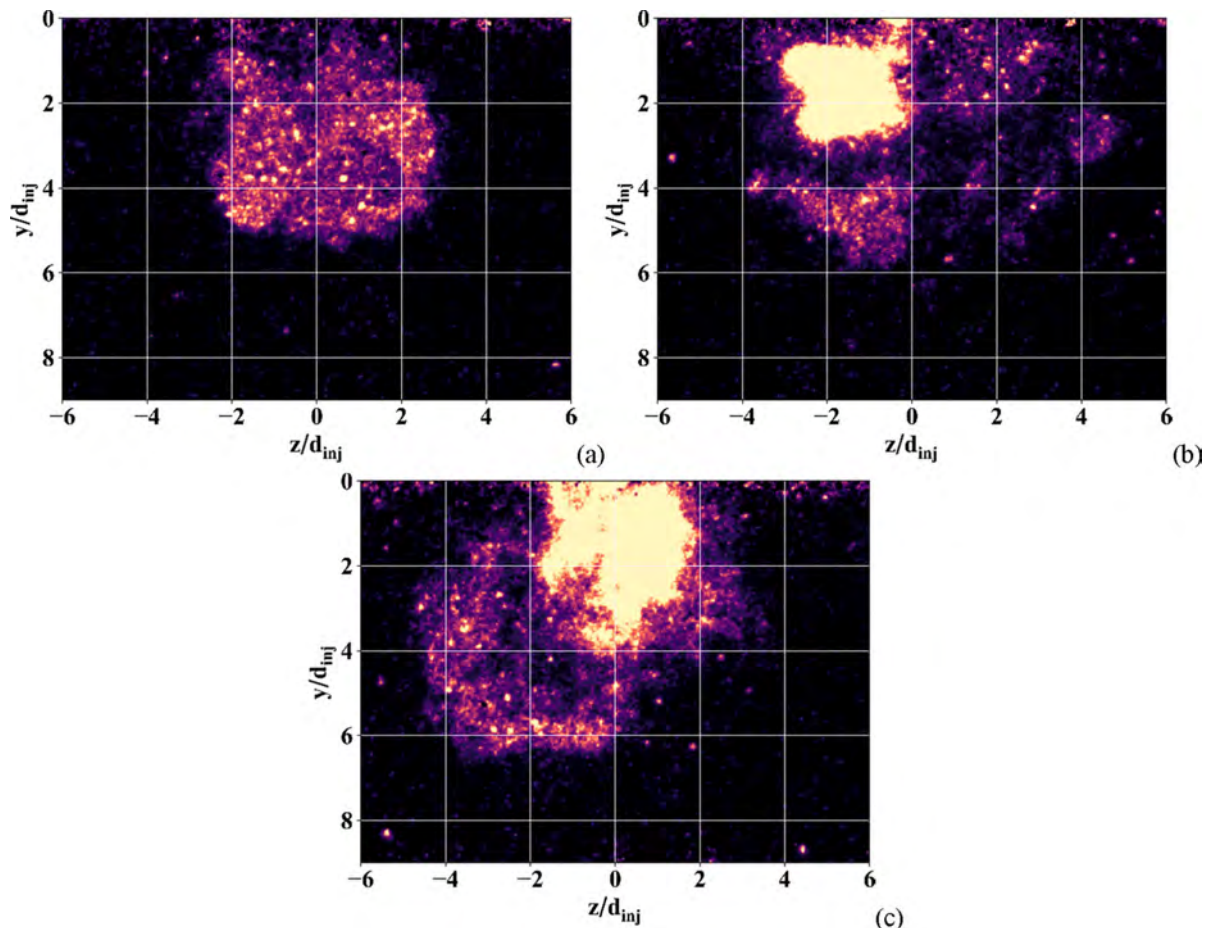
Fig. 10. Spanwise PLIF images collected at x/d_{inj} = 23.4 downstream of PIMs at J = 2.1 where (a) shows a single shot baseline image and (b) and (c) show representative single-shot images of jet breakup after plasma impact.
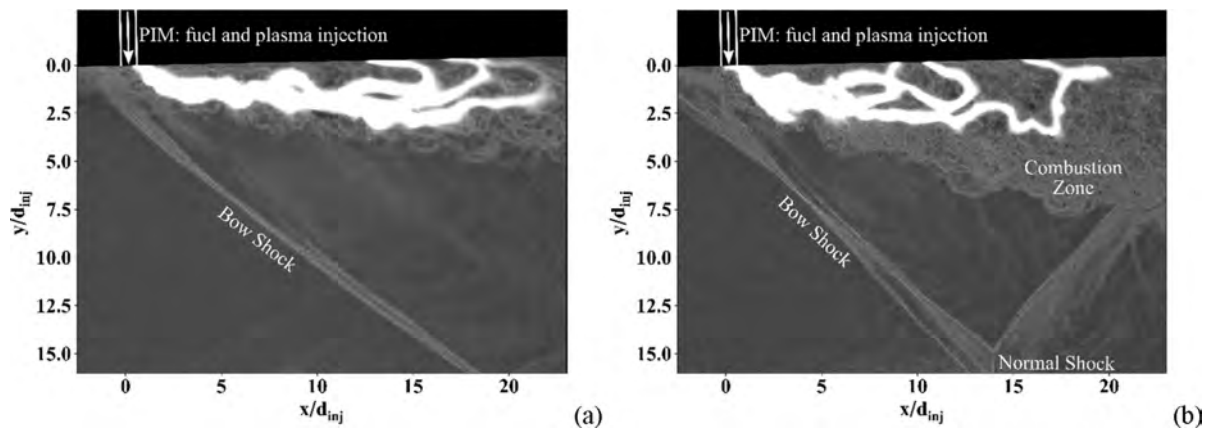
Fig. 11. Schlieren data with 3 PIMs operating where (a) shows a partial oxidation mode and (b) shows strong combustion.

combustion wedge protrudes deeper into the coreflow, upstream separation in front of the PIMs has increased, and a normal shock sits around $x/d_{inj} \approx 14$, producing a strong bottom wall separation region and corresponding shock.

Pressure distributions across the top wall of the test section also illustrate differences in combustion mode. In Fig. 12a, pressure distributions at three cases are shown: baseline flow, three PIM fueling, and three PIM fueling after extended (t > 10 ms) plasma actuation. The last case, where a significant and extended pressure rise is seen downstream of the PIMs, is termed strong combustion due to this effect on the flowfield. The high heat release from chemical reactions initiated and sustained by plasma interaction causes flow separation and the formation of a subsonic "combustion wedge" which acts as a virtual obstacle in the flowfield leading to modification of the stagnation pressure distribution. In Fig. 12b, the stagnation pressure measured at the end of the test section decreases near the top wall with combustion and increases near the bottom wall. While the strong combustion wedge on the top wall produces this redistribution of pressure, numerical integration across pitot-rake pressures produces a constant area under the curve.

Development of the strong combustion pattern presented in Fig. 12 at the fueling + plasma case requires both the proper initial flowfield and PIM conditions (fueling, plasma power, stagnation conditions, etc.) and some time for plasma elongation and interaction with the fuel jet. After plasma is actuated on, and before flowfield transition to a strong combustion mode, partial oxidation of the fuel jet produces weak heat release in a downstream reaction zone. When heat release in the downstream zone becomes sufficient, flow separation occurs and rapidly moves upstream to stabilize at the PIM locations. More details on the

mechanism of flowfield transition and resulting instabilities are presented in [32,20].

High-speed color images were collected of the plasma and flame pattern, where the purple in images is caused from the second positive system of nitrogen ($C^3\Pi_u \to B^3\Pi_g$), and the blue is due to chemical reactions in fuel producing emission from CN* ($B^2\Sigma^+ \to X^2\Sigma^+$) and CH* ($A^2\Delta \to X^2\Pi$) among others. Fig. 13a and b show spanwise images collected through the vacuum port window illustrating differences in plasma filament structure before and after the transition to strong combustion. In Fig. 13a, plasma filament path lengths do not extend much in the z-direction and filaments do not penetrate very far into the core flow, but rather remain located within the fuel jets. In Fig. 13b, the strong combustion wedge has formed, and this produces a significant separation region resulting in greater filament penetration in the y-direction. An upstream portion of the filaments locate within the fuel jet, but downstream tail portions are in a lean environment, as seen by the change in color.

Similar conclusions are produced from wall normal chemiluminescent imaging of the two combustion modes, as shown in Fig. 13c,d. Before strong combustion occurs, elongated filaments, located largely in the fuel jets, produce contained streamwise chemiluminescent reaction zones downstream. When flow transition occurs, plasma filaments become trapped in the separation bubble, and fuel in this separation bubble produces a dispersed downstream flame pattern.

4.2. Fuel pattern at combustion

The fuel pattern in the separation region formed near the PIMs with
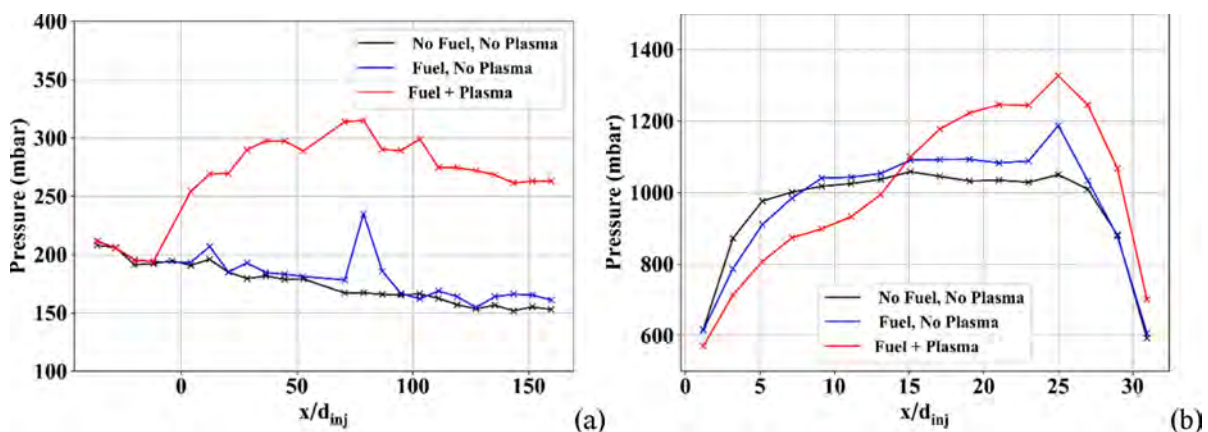

Fig. 12. Three PIM operation pressure distributions (a) shows the static pressure distribution on the top wall at three cases and (b) shows the total pressure distribution at the end of the test section at three cases.
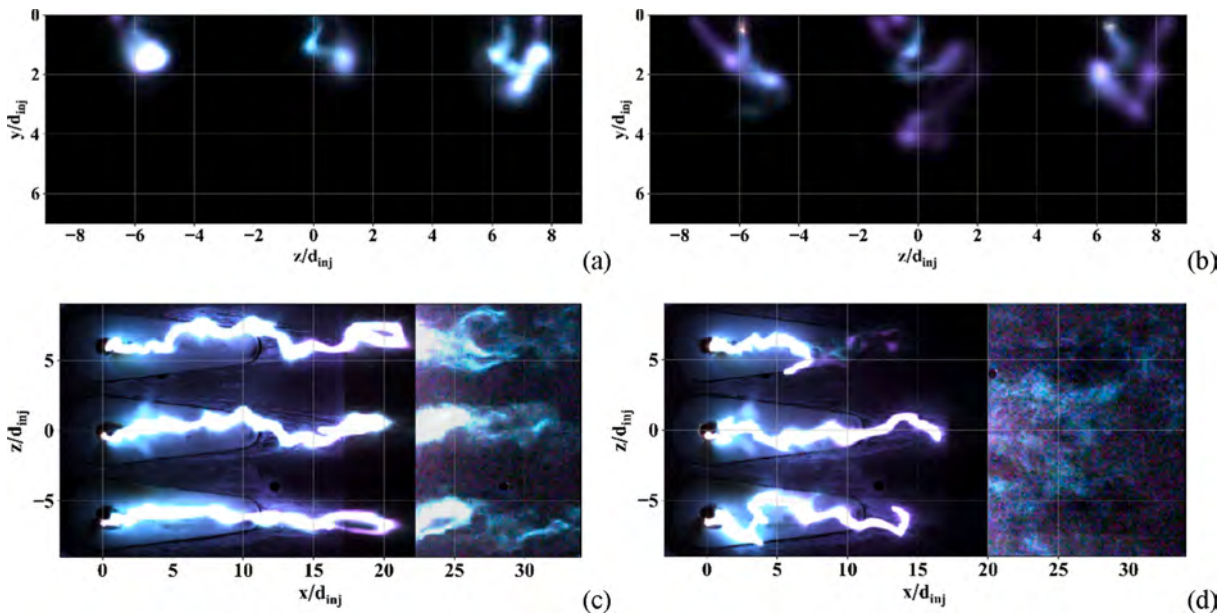
Fig. 13. Enhanced color images of the three PIM plasma pattern where (a)(c) show partial oxidation and (b)(d) show strong combustion. The images brightness is enhanced at $x/d_{inj} > 22$ (c) and $x/d_{inj} > 20$ (d).

strong combustion was mapped using acetone PLIF images collected at different delay times after the electrical discharge was turned off. Short intensifier gating was arranged, $t_{exp} = 20$ ns, so flame luminescence was discriminated to the level of the image background. This way PLIF images of the fuel distribution could be collected during combustion. Raw images were normalized by laser sheet characterization images collected at uniform acetone seeding without flow, and image processing was

performed to extract the area occupied by fuel in each image. This was done by using a gaussian filter with $\sigma = 3$ to reduce photon shot noise then summing over pixels exceeding 5 times the image background. Images were collected at two cases: (1) at varying image delay time after a fixed plasma pulse duration of 10 ms and strong combustion, and (2) at a fixed image delay time after plasma was terminated with a varying plasma pulse duration. These two cases were evaluated to assess the time
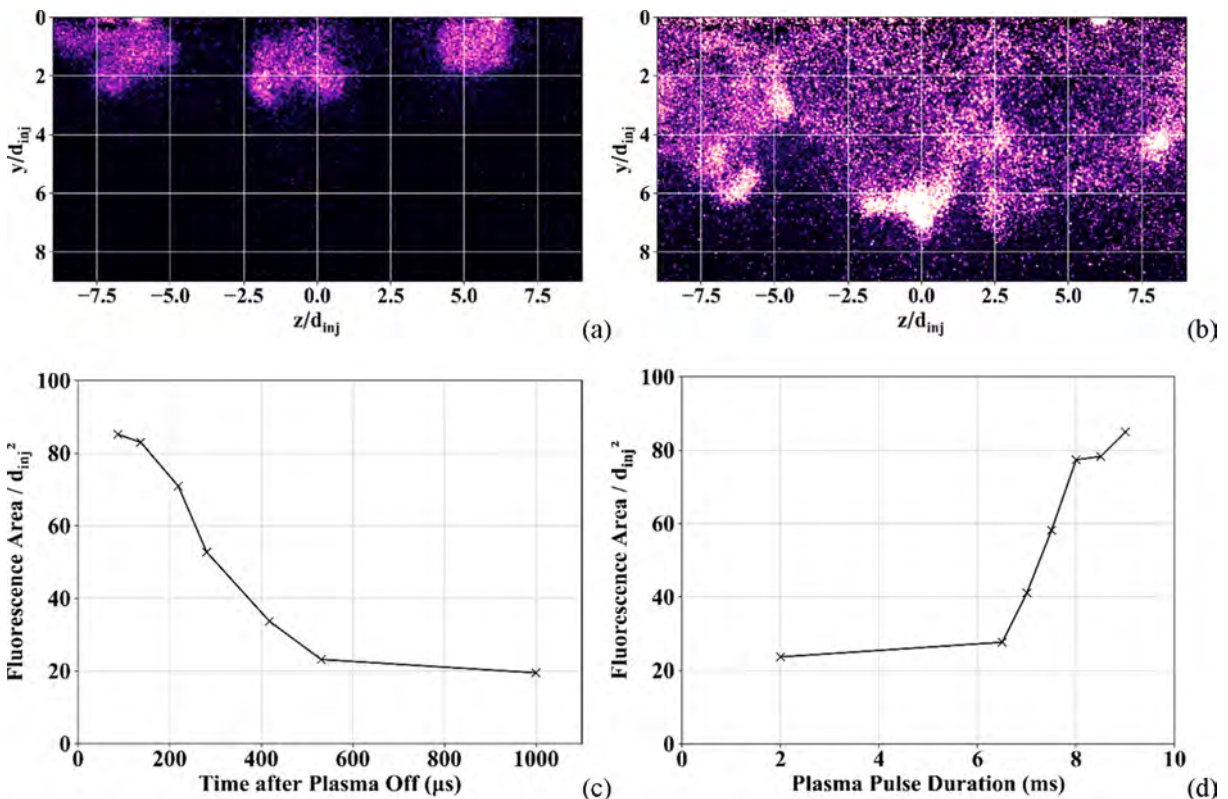

Fig. 14. Acetone PLIF results at 3 PIM combustion tests where (a) shows baseline fueling with no plasma, (b) shows 100 μs after strong combustion, (c) shows the occupied fuel area at varying delays after a 10 ms plasma pulse and (d) shows the occupied fuel area 150 μs after plasma at varying plasma duration.

for the flowfield to return to the baseline fueling case and to determine the plasma pulse duration to transition the flowfield to strong combustion. In Fig. 14a and b acetone PLIF images are presented collected at a spanwise laser sheet position of $x/d_{inj} = 15.6$ at baseline flow and 80 μs after extended ($t_{pulse} = 10$ ms) plasma impact. At baseline conditions with fuel injection but no plasma (see Fig. 14a) three distinct jets are visible with relatively small penetration into the flow. In Fig. 14b, collected after sustained plasma impact has transitioned the flowfield, a high concentration of fuel is seen widely distributed in the spanwise direction and penetrating deep into the core flow. This indicates that, with strong combustion, over-fueling occurs in the separation bubble due to its localization over the PIM fueling ports and reduced turnover time. As time after plasma-off increases, this separation region decays back to baseline flow because heat release from chemical reactions is insufficient to sustain this flow separation without energy addition from plasma. The time of this decay is shown in Fig. 14c, where at about 500 μs after plasma is terminated, the fuel area is near the baseline case.

The minimum plasma duration needed to transition the flow pattern to a strong combustion mode was similarly evaluated. A series of images was collected at the same delay time after plasma, $t_{delay} = 150$ μs, but at plasma durations $t_{pulse} = 2$–9 ms. The fuel area was then calculated. In Fig. 14d it is seen that a plasma pulse duration $t_{pulse} = 0$–6.5 ms is insufficient to transition the flowfield, and between 6.5 ms and 8 ms pulse duration there is a sharp gradient in the occupied fuel area that corresponds to the rapid upstream movement of the separation region. At the described operational parameters, a minimum plasma pulse duration of $t_{pulse} = 8$ ms is required for ignition of the fuel air mixture, upstream movement of the separation bubble, and fuel distribution within that separated region.

5. Discussion

Single-PIM test results demonstrated that plasma actuation produced a distinct mixing pattern with reduced PLIF signal measured from the plasma-occupying or post-plasma regions. Enhanced mixing is determined from the improved penetration and expansion of the jet, as well as the fuel jet breakup. There are several mechanisms, listed below, which might be responsible for producing these changes which favor combustion intensification. All of them result from the intense localized gas heating within the plasma filaments. Both direct and indirect mechanisms of plasma-flow interaction are responsible for improvements to jet expansion and mixing.

(1) Volumetric expansion of the gas heated by plasma impact leads to an on-average increase in the fuel jet cross-section. Assuming isobaric conditions, the volumetric expansion could be simply estimated as follows:

$$\frac{\Delta V_i}{V_i} = \frac{\Delta T_g}{T_g} = \frac{W_{pl}}{c_p \bullet \dot{m}_i \bullet T_g} \tag{2}$$

where V_i is the volume associated with the heating (near-wall jet section corresponding to a low PLIF signal), and $\dot{m}^i$ is the gas flow rate through this section. Such an estimate produces ΔT_g 40*K* as the average heating across the jet cross-section, leading to a ∼ 14% difference in the static temperature in the area. As the plasma mainly locates within the fuel jet, expansion of the fuel jet increases fuel–air interaction surfaces. Comparing this value to the average volumetric expansion measured by PLIF and indicated in Table 1 indicates that this mechanism is a leading cause of substantial mixing enhancement, but alone is not responsible.

(2) As a result of plasma-based energy deposition, flow structures at different scales are modified, from small-scale structures near the fuel-jet nozzle to major shock structures. This occurs due to the localized nature of the gas heating, which has a similar effect as a solid obstacle in the flow, increasing the pressure in front of it. This effect is insignificant with single-PIM operation, see Fig. 5. However, with three PIMs as shown in Fig. 11, plasma heating and additional energy release from

chemical reactions lead to amplification of the bow shock wave, which shifts the reflected shock wave upstream and, in turn, affects the combustion zone. A more sophisticated mechanism is also realized in a supersonic flow: at strong non-homogeneous thermal energy deposition, the sonic velocity in this zone exceeds the flow velocity in the surrounding area, leading to the generation of a subsonic flow zone within the supersonic one. This causes a significant pressure redistribution in the flowfield [38] affecting the flow structure on both micro- and macroscales. Specifically, the jet and surrounding features, such as the barrel shock at the jet exit, are modified due to the formation of a subsonic plasma channel anchored through the shock structure, coupling the jet-exit conditions to the flowfield.

Modification of the barrel shock structure at plasma impact might be an important mechanism for mixing enhancement. Fig. 15 shows differences in the barrel shock structure due to plasma impact, where at plasma actuation the barrel shock is shorter, wider, and more lifted in the flow. Previous studies [39,7] on transverse injection into supersonic flows have indicated that the development of large-scale coherent vortices may be highly sensitive to oscillations in the Mach disk, and the main path of injected gas oscillates between the Mach disk and the upstream surface of the barrel shock. In the latter case, high velocity fluid interacts at the jet boundary with the cross flow, generating high shear and large-scale vortices. Changes to the barrel shock structure due to plasma actuation require more detailed study of the flow coupling plasma provides and the impact this has on the downstream development of the injected jet.

(3) Thermal cracking/molecular dissociation of the fuel-acetone-air mixture due to plasma impact readily explains the decreased PLIF signal in the plasma region, observed in Fig. 7. This also increases the gas pressure due to increased number density $P = \sum_i N_i \bullet kT_i$ which aids with expansion. Preconditioning of the fuel, e.g., via dissociation due to thermal non-equilibrium processes, is an additional benefit for combustion.

(4) Excitation of flow instabilities and generation of extra vorticity are indirect mechanisms of mixing enhancement. The first is realized through the Richtmyer-Meshkov instability [40,41], occurring in flows with non-collinear gradients of gas density and pressure. This leads to formation of deterministic vortex-dominated flows, and subsequently, to small-scale stochastic perturbations resulting in accelerated interfacial stretching and turbulent kinematic mixing. Gas diffusion finalizes mixing on the molecular level.

The dynamics of vorticity, ω, can be described by taking the curl of the Navier-Stokes momentum equation yielding:

$$D\omega/Dt = -\omega(\nabla \cdot V) + 1/\rho^2 \cdot (\nabla\rho \times \nabla P) + (\omega \cdot \nabla)V + 1/\text{Re} \cdot (\nabla^2 \cdot \omega) + \nabla \times B \tag{3}$$

where the terms on the right describe 1) expansion, 2) baroclinic torque, 3) vortex stretching, 4) viscous diffusion, and 5) external body forces. The baroclinic term is an essential source of "new" vorticity and is the most important for the further consideration. To briefly estimate the magnitude of the baroclinic term, a basic scheme could be considered characterized by wall injection of gaseous fuel into a compressible flow with an electrical discharge along the fuel jet. In the area located near the fuel jet nozzle, a pressure gradient is generated due to the interaction of the main flow and the transverse jet. Near the wall, where the plasma situates inside of the fuel jet, a gas density gradient is generated by gradual electrical energy deposition along the fuel jet. This effect is amplified by molecular dissociation of the fuel. The thermal effect on gas density can be expressed by deriving the equation of state,

$$\rho = \frac{\mu \bullet P}{R \bullet T}, \nabla\rho = -\frac{\mu \bullet P}{R} \bullet \frac{1}{T^2} \bullet \frac{\partial T}{\partial x} + \frac{P}{R \bullet T} \bullet \frac{\partial \mu}{\partial x}$$
$$= \frac{\mu \bullet P}{R \bullet T \bullet U} \bullet (\frac{1}{\mu} \bullet \frac{\partial \mu}{\partial t} - \frac{1}{T} \bullet \frac{\partial T}{\partial t}) \tag{4}$$

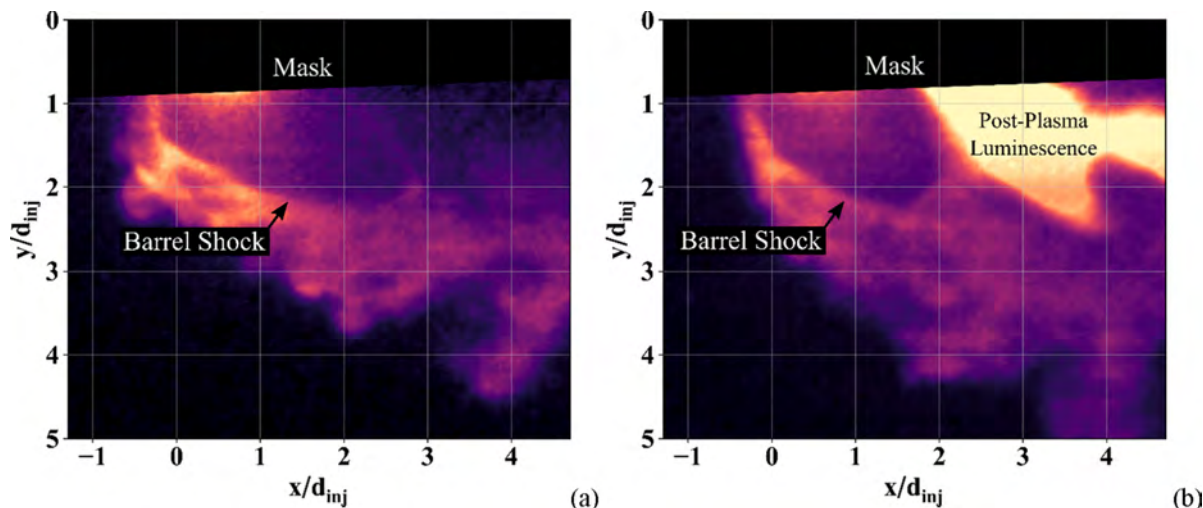where μ is the molar mass, *R* is the universal gas constant, and *U* is

Fig. 15. Acetone PLIF images of a single PIM ethylene-methane fuel jet at J = 2.1 illustrating barrel shock differences where (a) shows a jet before plasma and (b) shows a jet after plasma impact.

the gas velocity. Temperature dynamics, $\frac{\partial T}{\partial t}$, can be estimated using the plasma power W_{pl} deposition and fuel mass flow rate $\dot{m}^f$.

$$\frac{\partial T}{\partial t} = \frac{W_{pl} \bullet U}{c_{p\bullet} \bullet \dot{m}_f \bullet L} \tag{5}$$

For typical experimental conditions, W_{pl} = 3–5 kW; U = 500 m/s; $\dot{m}^f$ = 4 g/s; L = 2–5 cm, the temperature growth is $\frac{\partial T}{\partial t} \approx 10^7 \frac{K}{s}$. Following the suggestions above, the baroclinic term can be estimated to be as high as $D\omega/Dt = 1/\rho^2 \cdot (\nabla \rho \times \nabla P) \approx 10^8 - 10^9 1/s^2$, which might effectively act on a typical time scale of $\tau \approx 10^{-4}$ s.

Natural vorticity (generated without plasma due to the flow – fuel jet interaction) and plasma-induced vorticity affect the plasma filament flowpath by forming the plasma filament shape and moving the plasma towards the core flow. A previous study of the plasma filament structure with PIM actuation [18] showed significant influence of the counter-rotating vortex pair generated by the injected fuel-jet on the filament breakdown path. Plasma coupling to vortical structures in the flow and high volumetric expansion of the plasma, in turn, leads to kinematic displacement of flow in these structures, producing vorticity. The highly oscillatory nature of the PIM system introduces high-frequency sources of these turbulent channels into the developing gas stream, leading to jet breakup. Additionally, previous studies demonstrated strong turbulence developed from the cooling of post discharge gas channels [20].

In the case of turbulent combustion, the effective flame propagation velocity increases significantly due to an important role convection plays in energy/molecular species transport from the heat release region to the undisturbed flammable mixture. In contemporary combustion chambers including those of turbojets, ramjets, and scramjets, combustion starts in partially mixed flow where the fuel/oxidant ratio varies significantly across the working volume. In this diffusive combustion mode, combustion and mixing can develop simultaneously affecting each other [42,43]. The molecular level of mixing through collisions is provided by conventional molecular diffusion. However, molecular diffusion is very slow when compared to the available mixing time, which is limited by residence time in the combustion zone. The characteristic thickness of such a layer may be estimated by $\approx \sqrt{Dt}$, where D and t are the diffusion coefficient and time of interaction, respectively. Mechanisms of natural or artificial interfacial stretching accelerate the mixing process [44] and reduce length scales over which combustion occurs.

Acetone PLIF imaging of the fuel distribution after PIM stabilized combustion revealed a significant fuel redistribution occurring in the separation region located at the fuel injection ports, the decay of this

separation region, and the minimum plasma pulse duration to initiate flowfield transition from partial oxidation to strong combustion. The sequence of flowfield transition and resulting dynamic instabilities at plasma actuation is presented in more detail in [32] but is briefly outlined as follows: (1) plasma stimulated reactions initiate combustion downstream of the PIM arrangement in fuel-rich areas inducing flow separation, (2) the separation zone moves upstream and reaches the PIMs, (3) the separation zone traps the plasma filaments and injected fuel, leading to a decrease in plasma power and equivalence ratio over the ignition limit, (4) this produces a decrease in chemical power, decreased separation zone size and partial restoration of the baseline flow before the cycle repeats [20]. The current PLIF measurements demonstrate the role over-fueling in the separation zone, and plasma-induced ignition and flow structure establishment have in the process of the dynamic instability in the combustor. Plasma-induced ignition and flowfield transition is particularly dominant as this process takes the longest time. This insight is important to develop methods to mitigate the onset of this combustion instability, which may require a redistribution of the electrical discharge in the combustor.

6. Conclusions

This work examined the mixing and flameholding characteristics of a plasma-stimulated model supersonic combustor. The technique employed couples a filamentary Q-DC electrical discharge to the fuel injection port in a so-called Plasma Injection Module or PIM, providing plasma localization within the fuel–air mixing layer. Acetone PLIF visualization was applied in this study along with multipoint static and Pitot pressure measurements, plasma characterization, schlieren imaging, and high-speed imaging. PLIF images were acquired at both streamwise and spanwise laser sheet orientations, and acetone was seeded into the gaseous fuel stream as a tracer. Two main configurations were explored: (1) a single PIM for studying mixing and (2) a three-PIM configuration for studying flameholding.

In the mixing study (employing a single PIM), the plasma was found to increase penetration, expansion, and breakup of the fuel-jet. On-average, volumetric expansion of the fuel jet is well explained by thermal addition from the plasma; however, fuel jet breakup is caused by the development of shear layer instabilities and the generation/amplification of vortical gasdynamic structures concomitant with the fuel jet and filamentary plasma.

In the flameholding study (employing three PIMs), the PLIF technique was applied to study the dynamics of the reaction zone formation and extinction. It was found that under the conditions of the current test,

the time to establish the combustion pattern corresponds to the formation of a flow separation zone behind the PIMs, and takes $t_{pulse} \approx 8$ ms. The gas pressure in this separation zone significantly increases due to chemical reactions. However, PLIF data indicates the concentration of unburned fuel in the plasma-supported separation zone remains high. Details of the chemical processes in the vicinity of the PIMs still need to be clarified. After the electric discharge is turned off, restoration of the initial flow pattern occurs in $t_{delay} < 1$ ms.

The current study, including acetone PLIF imaging, reveals important details regarding plasma-based supersonic mixing and flame-holding, such as fuel-jet breakup and ignition dynamics. It was performed in a plane wall geometry with direct transverse fuel injection and without mechanical flameholding elements. Practical implementation of such a geometry could deliver additional benefits due to potential reduction of pressure losses. Investigation of additional details is underway, requiring multiple species detection and quantification, and development of active control schemes to suppress combustion instabilities produced in the combustor.

CRediT authorship contribution statement

Skye Elliott: Methodology, Investigation, Formal analysis, Writing – original draft. **Philip Lax:** Investigation. **Sergey B Leonov:** Funding acquisition, Conceptualization, Writing – original draft. **Campbell Carter:** Writing – review & editing. **Timothy Ombrello:** Writing – review & editing.

Declaration of Competing Interest

The authors declare that they have no known competing financial interests or personal relationships that could have appeared to influence the work reported in this paper.

Acknowledgments

References

[1] Q. Liu, D. Baccarella, T. Lee, Review of combustion stabilization for hypersonic airbreathing propulsion, Prog. Aerosp. Sci. 119 (November 2020), 100636.

[2] J. Urzay, Supersonic Combustion in Air-Breathing Propulsion Systems for Hypersonic Flight, Annu. Rev. Fluid Mech. 50 (1) (2018) 593–627.

[3] J.C. Poster, P.I. King, M.R. Gruber, C.D. Carter, M.D. Ryan, K.Y. Hsu, In-stream hypermixer fueling pylons in supersonic flow, J. Propul. Power 25 (4) (2009) 885–901.

[4] K.Y. Hsu, C.D. Carter, M.R. Gruber, T. Barhorst, S. Smith, Experimental study of cavity-strut combustion in supersonic flow, J. Propul. Power 26 (6) (2010) 1237–1246.

[5] F.W. Barnes, C. Segal, Cavity-based flameholding for chemically-reacting supersonic flows, Prog. Aerosp. Sci. 76 (July 2015) 24–41.

[6] A. Ben-Yakar, R.K. Hanson, Cavity Flame-Holders for Ignition and Flame Stabilization in Scramjets: An Overview, J. Propul. Power 17 (4) (2001) 869–877.

[7] K. Mahesh, The Interaction of Jets with Crossflow, Annu. Rev. Fluid Mech. 45 (1) (2013) 379–407.

[8] D.W. Bogdanoff, Advanced injection and mixing techniques for scramjet combustors, J. Propul. Power 10 (2) (1994) 183–190.

[9] S. Leonov, V. Bityurin, K. Savelkin, D. Yarantsev, Progress in Investigation for Plasma Control of Duct-Driven Flows. in *41st Aerospace Sciences Meeting and Exhibit*, 2003.

[10] K. Savelkin, D. Yarantsev and S. B. Leonov, "Experiments on Plasma-Assisted Combustion in a Supersonic Flow : Optimization of Plasma Position in Relation to the Fuel Injector," *Aerospace Lab, Plasmas for Aeronautics,* vol. 10, 2015.

[11] S. Leonov, A. Houpt, S. Elliott, B. Hedlund, Ethylene Ignition and Flameholding by Electrical Discharge in Supersonic Combustor, J. Propul. Power 34 (2) (2018) 499–509.

[12] A.W. Vreman, N.D. Sandham, K.H. Luo, Compressible mixing layer growth rate and turbulence characteristics, J. Fluid Mech. 320 (1996) 235–258.

[13] M.R. Gruber, A.S. Nejad, T.H. Chen, J.C. Dutton, Compressibility effects in supersonic transverse injection flowfields, Phys. Fluids 9 (5) (1997) 1448–1461.

[14] P. José, M. Ferrer, G. Lehnasch, A. Mura, Compressibility and heat release effects in high-speed reactive mixing layers I.: Growth rates and turbulence characteristics, Combust. Flame 180 (2017) 284–303.

[15] J.M. Seiner, S.M. Dash, D.C. Kenzakowski, Historical Survey on Enhanced Mixing in Scramjet Engines, J. Propul. Power 17 (November 2001) 1273–1286.

[16] N.J. Williams, T.M. Moeller, R.J. Thompson, Numerical simulations of high frequency transverse pulsed jet injection into a supersonic crossflow, Aerosp. Sci. Technol. 103 (August 2020), 105908.

[17] M.D. Dziuba, T. Rossmann, Mixing Enhancement of Modulated Transverse Sonic Jets in a Supersonic Crossflow, J. Propul. Power 35 (3) (2019) 669–674.

[18] B.S. Leonov, B. Hedlund, A. Houpt, Morphology of Quasi-Direct-Current Discharges Collocated with Fuel Jets in a Supersonic Crossflow, J. Propul. Power 36 (4) (2020) 508–516.

[19] A. Firsov, K.V. Savelkin, D.A. Yarantsev, S.B. Leonov, Plasma-enhanced mixing and flameholding in supersonic flow, Phil. Trans. R. Soc. A. 373 (2048) (2015) 20140337.

[20] S. Leonov, Electrically Driven Supersonic Combustion, Energies 11 (7) (2018) 1733.

[21] R.K. Hanson, J.M. Seitzman, P.H. Paul, Planar laser-fluorescence imaging of combustion gases, Applied Physics B Photophysics and Laser Chemistry 50 (6) (1990) 441–454.

[22] A. Cessou, U. Meier, D. Stepowski, Applications of planar laser induced fluorescence in turbulent reacting flows, Meas. Sci. Technol. 11 (7) (2000) 887–901.

[23] L.S. Jacobsen, C.D. Carter, R.A. Baurle, T.A. Jackson, S. Williams, D. Bivolaru, S. Kuo, J. Barnett, C.-J. Tam, Plasma-Assisted Ignition in Scramjets, J. Propul. Power 24 (4) (2008) 641–654.

[24] R. Hruschka, S. O'Byrne, H. Kleine, Comparison of velocity and temperature measurements with simulations in a hypersonic wake flow, Exp. Fluids 51 (2) (2011) 407–421.

[25] C. Schulz, V. Sick, Tracer-LIF diagnostics: Quantitative measurement of fuel concentration, temperature and fuel/air ratio in practical combustion systems, Prog. Energy Combust. Sci. 31 (1) (2005) 75–121.

[26] L.M. Cantu, E.C. Gallo, A.D. Cutler, B.F. Bathel, P.M. Danehy, R.D. Rockwell, C. P. Goyne, J.C. McDaniel, Visualization of simulated fuel-air mixing in a dual-mode scramjet, J. Propul. Power 32 (2) (2016) 373–382.

[27] G.M. Breuer, E.K.C. Lee, Fluorescence decay times of cyclic ketones, acetone, and butanal in the gas phase, J. Phys. Chem. 75 (7) (1971) 989–990.

[28] A. Lozano, B. Yip, R.K. Hanson, Acetone: a tracer for concentration measurements in gaseous flows by planar laser-induced fluorescence, Exp. Fluids 13 (6) (1992) 369–376.

[29] B. Yip, M.F. Miller, A. Lozano, R.K. Hanson, A combined OH/acetone planar laser-induced fluorescence imaging technique for visualizing combusting flows, Exp. Fluids 17 (5) (1994) 330–336.

[30] R.A. Bryant, A. Ratner, J.F. Driscoll, "Using PLIF Determined Flame Structure to Analyze Supersonic Combustion Efficiencies," in *37th AIAA Aerospace Sciences Meeting and Exhibit*, Reno, NV, 1999.

[31] W.M. VanLerberghe, J.G. Santiago, J.C. Dutton, R.P. Lucht, Mixing of a sonic transverse jet injected into a supersonic flow, AIAA Journal 38 (3) (2000) 470–479.

[32] S. Elliott, A. Houpt and S. B. Leonov, "Instabilities of Supersonic Combustion at Plasma-Based Flameholding," in *AIAA Propulsion and Energy 2019 Forum, AIAA Paper #2019-*, Indianapolis, 2019.

[33] S.H. Mousavipour, P.D. Pacey, Initiation and abstraction reactions in the pyrolysis of acetone, J. Phys. Chem. 100 (1996) 3573–3579.

[34] M.C. Thurber, R.K. Hanson, Pressure and composition dependences of acetone laser-induced fluorescence with excitation at 248, 266, and 308 nm, Appl. Phys. B: Lasers Opt. 69 (3) (1999) 229–240.

[35] G. Pellet, S.N. Vaden, L. Wilson, Gaseous Surrogate Hydrocarbons for a HIFIRE Scramjet that Mimic Opposed Jet Extinction Limits for Cracked JP Fuels. in *55th JANNAF Propulsion Meeting*, 2008.

[36] M. Gamba, M.G. Mungal, Ignition, flame structure and near-wall burning in transverse hydrogen jets in supersonic crossflow, J. Fluid Mech. 780 (September 2015) 226–273.

[37] M. Sun, H. Wang, F. Xiao (Eds.), Jet in Supersonic Crossflow, Springer Singapore, Singapore, 2019.

[38] S. Elliott, M. Hasegawa, H. Sakaue, S. Leonov, Shock-Dominated Flow Control by Plasma Array: Pressure Analysis Including Pressure-Sensitive Paint Visualization, Exp. Therm Fluid Sci. (September 2021), 110522.

[39] S. Kawai and S. K. Lele, "Dynamics and mixing of a sonic jet in a supersonic turbulent crossflow," Stanford CA, 2009.

[40] A.A. Zheltovodov, E.A. Pimonov, Intensification of mixing of parallel compressible flows using a localized pulse-periodic energy supply, Technical Physical Letters 39 (November 2013) 1016–1018.

[41] C. Li, D.L. Book, Instability generated by acceleration due to rarefaction waves, Phys. Rev. A 43 (March 1991) 3153–3156.

[42] V.R. Kuznetsov, V.A. Sabelnikov, Turbulence and combustion, Hemisphere Pub. Corp, New York, 1990.

[43] P.A. Libby, F.A. Williams (Eds.), Turbulent reacting flows, Springer Verlag, Berlin New York, 1980.

[44] J.M. Ottino, The kinematics of mixing : stretching, chaos, and transport, Cambridge University Press, Cambridge New York, 1989.